AGU ADVANCING EARTH AND SPACE SCIENCE

Water Resources Research

RESEARCH ARTICLE
10.1029/2022WR032402

Special Section:
Modeling, simulation, and big data techniques in subsurface fluid flow and transport

Systematic Investigation of Corner Flow Impact in Forced Imbibition

Yang Liu[1,2], Steffen Berg[3], Yang Ju[4], Wei Wei[2], Jisheng Kou[5], and Jianchao Cai[1,2]

[1]State Key Laboratory of Petroleum Resources and Prospecting, China University of Petroleum, Beijing, China, [2]Institute of Geophysics and Geomatics, China University of Geosciences, Wuhan, China, [3]Shell Global Solutions International B.V., Amsterdam, The Netherlands, [4]State Key Laboratory of Coal Resources and Safe Mining, China University of Mining and Technology, Beijing, China, [5]School of Mathematics and Statistics, Hubei Engineering University, Xiaogan, China

Key Points:

- Pore-scale simulation of forced imbibition in natural rock is performed at four different injection rates
- The pore filling event that dominates imbibition shifts from ganglion dynamics to snap-off trapping as the injection flow rate decreases
- Pore filling events and displacement patterns significantly affect fluid structure and distribution

Supporting Information:

Supporting Information may be found in the online version of this article.

Correspondence to:

J. Cai,
caijc@cup.edu.cn

Citation:

Liu, Y., Berg, S., Ju, Y., Wei, W., Kou, J., & Cai, J. (2022). Systematic investigation of corner flow impact in forced imbibition. *Water Resources Research*, *58*, e2022WR032402. https://doi.org/10.1029/2022WR032402

Received 18 MAR 2022
Accepted 20 SEP 2022

Abstract Imbibition in porous media plays a crucial role in many engineering and industrial processes, such as enhanced oil recovery and groundwater contamination remediation. Due to the instabilities at the two-phase interface, the defending fluids in these processes are often not effectively displaced. Therefore, it is of great significance to study imbibition in natural rocks at the pore scale, especially under the completely wetting and viscously unfavorable conditions due to their contribution to interfacial instability. In this work, numerical simulations of forced imbibition in three natural rocks are carried out at four different injection rates based on the color lattice Boltzmann model. The interfacial evolution and in situ fluid distribution are analyzed from several perspectives. Results show that as the capillary number, expressed in logarithms, varies from −2.5 to −4.0, the flow characteristics of the invading fluid change from leading films on the solid surface of large pores to corner flow along the pore corners of pores with different sizes, the dominant pore filling event changes from ganglion dynamics to snap-off trapping, and the morphology of the displacement front changes from viscous fingering to a rough but uniform characteristic. These changes at the two-phase interface determine the fluid distribution and fluid structure, controlling the microscopic displacement efficiency, interface area and fluid connectivity. This work systematically investigates for imbibition of the local and global flow physics and dynamics, the mechanical nature and the resulting effects of interfacial instability under unfavorable conditions, which help to deepen our understanding of the microscopic mechanism of forced imbibition.

Plain Language Summary Pore-scale simulations are performed in this work to investigate two-phase flow within natural rocks under a completely wetting condition. Results show that the displacement process, in terms of pore filling dynamics and the evolution of the whole displacement front, varies significantly at different injection flow rates. These differences were first analyzed qualitatively based on flow characteristics and fluid interface morphology, and then their impact on overall displacement was characterized from multiple perspectives, including nonwetting fluid recovery, two-phase fluid distribution, and fluid structure. These results on the complex interfacial dynamics and fluid distribution characteristics within the pore space provide a theoretical basis for the application of two-phase flow in engineering activities such as petroleum resource development.

1. Introduction

Immiscible fluid displacement in porous media is widespread in nature, and it plays an essential role in a variety of engineering and industrial processes, such as oil resource development (Abdallah et al., 2007; Cai, Wood, et al., 2022) and groundwater contamination remediation (Singh & Niven, 2013). Due to the instability of the fluid-fluid interface, incompact displacement patterns and incomplete pore fillings may be formed during these processes, resulting in a low microscopic displacement efficiency, which affects hydrocarbon recovery and groundwater purification (Y. Liu et al., 2019; Singh et al., 2019). Therefore, it is of great benefit to these fields to understand the flow physics and in situ fluid distribution within the pore space, especially under viscously unfavorable conditions where the displacement of a high-viscosity fluid by a low-viscosity one is accompanied by more complex interfacial dynamics.

The instability of the fluid-fluid interface and the complexity of the pore space make the two-phase flow in porous media have characteristics such as rich flow physics and complex interface dynamics (Blunt, 2017; Mohanty

et al., 1987; Morrow, 1970; Singh et al., 2019). Since the pore-scale flow physics and dynamics determine macroscopic transport properties such as relative permeability, capillary pressure, and recovery curves, various studies on fluids distribution and interface evolution during two-phase flow in porous media have been carried out, with special attention to the overall and local morphological characteristics of fluid fronts and their evolutionary dynamics, as well as the time-dependent variation of two-phase fluid structure (Armstrong & Berg, 2013; Diao et al., 2021; Khanamiri & Torsæter, 2018; H. Liu et al., 2020; Schlüter et al., 2016). Despite the great progress in these fields, we still do not have a full grasp of all the interfacial evolution characteristics and their dynamics of the two-phase flow in porous media which become prohibitive for a consistent upscaling multiphase flow from pore to Darcy scale. For example, with the development of in situ imaging technology, some new transport phenomena, such as intermittent flow, flow dynamics of connected, and isolated fluids (Gao et al., 2021; Spurin et al., 2021; Y. Zhang et al., 2021), are being detected under the reservoir temperature and pressure conditions (Armstrong et al., 2016; Pak et al., 2015; Ruecker et al., 2015; Spurin et al., 2021). Therefore, fast interfacial dynamics at the pore scale still needs further exploration.

The displacement pattern during two-phase flow in porous media, based on the morphological characteristics of the fluid fronts, compact or noncompact, smooth or ramified, is classified as fingering and stable displacement. The critical flow conditions corresponding to different displacement patterns, including capillary fingering, viscous fingering, and stable displacement, are visually represented by the phase diagram with two dimensionless parameters, that is, capillary number and viscosity ratio M (Lenormand et al., 1988). Within this basic framework, current studies attempt to build a comprehensive phase diagram with a wider range of applicability and more precise regional boundaries by considering a variety of factors such as pore structure, fluid properties, wettability, and flow conditions (Chen et al., 2018; Michels et al., 2021; Tsuji et al., 2016; C. Zhang et al., 2011). Since the whole fluid front is composed of a large number of individual meniscus, some studies have attempted to reveal the origin of the different morphological characteristics of the two-phase interface in terms of the motion of the meniscus and their competition/cooperation between adjacent pores (Armstrong & Berg, 2013). Cieplak and Robbins (1988, 1990) proposed three modes of meniscus motion, including burst, touch, and overlap, to explain the shift from fingering to stable invasion for fluid fronts during capillary-dominated displacement. This trend has been confirmed in different experiments and numerical simulations (Bakhshian et al., 2020; Jung et al., 2016; Singh, Scholl, et al., 2017). However, the overall morphology of the displacement fronts in such studies is only the result of terminal meniscus motion because of the simple pore structure and smooth solid surface, as well as the wetting condition with large contact angles. When the invading fluid forms a smaller contact angle with the solid surface, some arc meniscus flow phenomena will be generated in the pore corners (corner flow) and within the surface rough structure (film-like flow) (Dong & Chatzis, 1995; Hu, Wan, et al., 2018; Zhao et al., 2016). The effect of the interaction between the arc and terminal meniscus motion on the overall fluid front, especially within a three-dimensional (3D) porous medium, is worthy of further exploration.

With the advances in fast synchrotron micro-tomography and direct numerical simulations, rapidly evolving interfaces during two-phase flow in 3D porous media can be captured in real time. Thus, their detailed dynamics and their effects on macroscopic physical properties are further revealed. Examples include ganglia fragmentation and coalescence during steady-state flow process (Armstrong et al., 2016; Reynolds et al., 2017), Haines jump and snap-off in unsteady-state flow process (Berg et al., 2013; Singh, Menke, et al., 2017; Zacharoudiou et al., 2018).

For the drainage process, the pore size distribution is the main geometrical factor dominating the flow due to the nature of the invading fluid (nonwetting fluid) flowing along the center of the pore space. This is one of the main reasons why the invasion-percolation theory and the pore network modeling can describe the drainage process well (Blunt, 2001; Wilkinson & Willemsen, 1983). In addition, the fact that the invading fluid remains well connected during the drainage process makes it easier to be detected by the available imaging techniques. Therefore, the fast interfacial dynamics associated with the drainage process has been relatively well studied. An example is the rapid fluid distribution and interfacial evolution during Haines jump, which involves redistribution of nonwetting fluids and retraction of wetting fluids, pinning-depinning interfaces at the throat, as well as Roof and distal (non-local) snap-offs (Alhosani et al., 2020; Herring et al., 2018; Roof, 1970).

For imbibition processes, we face a somewhat higher degree of complexity in terms of pore scale displacement dynamics while at the same time much less work has been published on that specific aspect in comparison with drainage. Imbibition processes are not just the inverse of drainage, that is, they are not just "symmetric"

to inversion of the phases. The asymmetry is introduced by wetting, that is, it makes a big difference whether a wetting phase displaces a nonwetting phase or the other way round. As a consequence there are conceptual differences between drainage and imbibition, from the perspective of pore scale mechanisms and their consequence for fluid topology and dynamics (Schlüter et al., 2016). An additional complication is that for the imbibition process, the evolution of fluid fronts is influenced not only by the pore structure but also by the pore corner and the rough structure on the solid surface due to the nature of the preferential flow of the invading fluid (wetting phase) along the solid surface (Cai et al., 2021; Geistlinger & Zulfiqar, 2020; Mohanty et al., 1987). Therefore, the flow phenomena in the imbibition process are relatively more complicated (Cai, Chen, et al., 2022; Lenormand, 1990). For example, the capillary valve effect and the pinning effect at the sharp protruding structures (high-curvature solid surfaces) make the invading fluid during the capillary-force dominated imbibition to fill the pores not simply in the order of pore size, from small to large (Wiklund & Uesaka, 2013; Wu et al., 2016; Xu et al., 2017). Under the condition that the invading fluid forms a small contact angle with the solid surface, a predominant film-like or corner flow is formed in front of the terminal interface, which expands and aggregates at the throat, thus triggering a snap off (Singh, Menke, et al., 2017). Therefore, the morphological characteristics of the fluid fronts during imbibition under this wetting condition are the result of a combination of piston-like interfaces and snap offs. Currently, most of the available experiments have focused on the snap-off dynamics caused by the corner or film-like flow when the capillary forces are fully dominant. The corner flow and snap-off dynamics and their effects on fluid fronts and fluid structures are of interest when the effects of viscous forces are still present and have different strengths.

Forced imbibition, especially under a fully wetting condition, has complex pore-scale flow physics due to additional interfacial dynamics, therefore, it is far from being possible to consider forced imbibition as simply the inverse process of drainage, even though both are two-phase fluid displacement processes (Meisenheimer et al., 2020; Porter et al., 2009; Schlüter et al., 2016). However, most studies in forced imbibition have generally been conducted in a certain water-wet range and have focused more on the evolution of piston-like fluid interfaces (Armstrong et al., 2014; Sergi et al., 2016). The corner flow dynamics during forced imbibition in natural porous media are poorly investigated, and the knowledge obtained based on ideal media models is far from being effective for flow problems in actual reservoir rocks with complex structures (Kubochkin & Gambaryan-Roisman, 2022; Sun, 2018). In addition, studies that combine pore-scale flow behaviors such as corner flow dynamics and displacement patterns during forced imbibition with quantitative descriptions of pore space have rarely been conducted.

Combining the digital rock technique and pore-scale direct numerical simulation method, this work focuses on the pore-scale imbibition behaviors in natural porous media under the completely wetting condition, and attempts to address the following two aspects: (a) The dominant flow physics and interfacial evolution dynamics within the pore space at different injection flow rates and (b) Quantitative characterization of the effects of corner flow and snap-off on interface evolution and fluid structure. The workflow of this study is organized in the following order. First, pore structure characteristics of the three rocks used are evaluated. Then, forced imbibition simulations based on the color lattice Boltzmann model are carried out. The interfacial evolution and in situ fluid distribution during the displacement process are comprehensively analyzed, including the displacement patterns, dominant force controlling the flow, microscopic displacement efficiency, two-phase fluid distribution, fluid connectivity, pore-filling events, and nonwetting fluids residual trapping.

2. Materials and Methods

2.1. Digital Rock Model

In this study, micro-CT images of three natural rocks, Bentheimer sandstone, Doddington sandstone, and Ketton carbonate, published on the Imperial College London website, are used to investigate the pore-scale flow mechanism during imbibition. Detailed petrophysical information on these three samples can be found in Raeini et al. (2017). After weighing the constraints such as computational resource consumption and representativeness of simulation results, a cubic subdomain with size 512^3 voxels is extracted from the original data set. The digital rock model used in subsequent imbibition simulations is obtained by further image processing of this subdomain, including removing isolated pores and coarsening voxels to twice the original resolution (Figure 1).

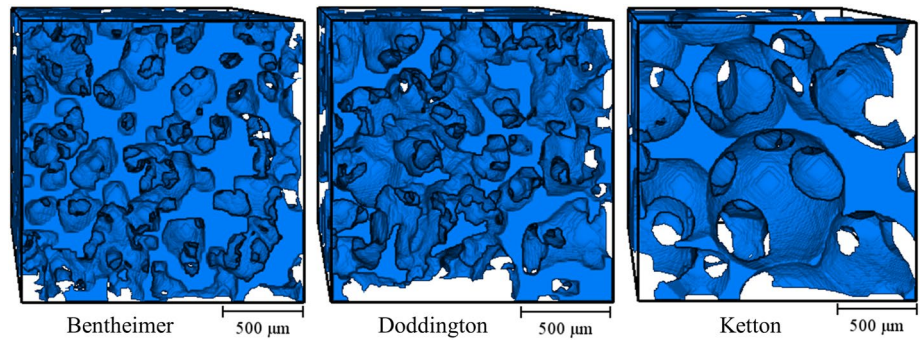

Figure 1. Digital rock model used in the simulation, where the pore structure is indicated in blue and rock skeleton is not shown.

In order to examine the differences between these three samples, the morphological and topological characteristics of pore structures are evaluated using the Minkowski functionals (Armstrong et al., 2019; Herring et al., 2013; Legland et al., 2007). Through a set of morphological descriptors defined by integral geometry, the Minkowski functionals can reflect the volume, area, curvature, and topology-related information of the spatial structure. Therefore, they are commonly used for pore structures to estimate their hydraulic parameters properties. For the 3D digital rock model, four Minkowski measurements (M_{0-3}) exist to characterize the geometric properties of the pore space and the pore-solid interface, respectively. M_0 measures pore volume with a dimension of [L^3], M_1 measures pore-solid interface area with a dimension of [L^2], M_2 measures integrated mean curvature with a dimension of [L]. M_3, a dimensionless number, measures integrated Gaussian curvature and is related to the Euler characteristic χ.

$$\chi = \frac{M_3}{4\pi} = \beta_0 - \beta_1 + \beta_2 \tag{1}$$

χ is a topological measurement that is often used to quantitatively evaluate the connectivity of pore structures, defined as the alternating sum of the number of discrete objects β_0, redundant connections β_1, and cavities β_2 present in the pore space. For consistency with previous work and to exclude the effect of sample size, porosity ϕ, specific interfacial area A_p, and mean curvature J, that is, M_{0-2} normalized by sample volume V, as well as the volume-normalized Euler characteristic $\chi_p = \chi/V$, are used in the present work.

Based on the binary data of the extracted model, the Minkowski measurements results of these three samples are shown in Table 1. Results show that the Bentheimer model has the largest pore space and pore-solid interface (maximum ϕ and A_p), and the highest connectivity (most negative χ_p), but its pore-solid interface has the highest degree of curvature (maximum J) among these three samples.

Table 1
Pore Structure Characteristics

Sample	Resolution	Minkowski measurements			
	d (μm)	ϕ (%)	A_p (μm^{-1})	J (μm^{-2})	χ_p (μm^{-3})
Bentheimer	3.0035	27.94	0.0140	1.27×10^{-5}	-3.00×10^{-7}
Doddington	2.6929	24.08	0.0109	1.24×10^{-5}	-1.55×10^{-7}
Ketton	3.00006	15.91	0.0049	5.07×10^{-6}	-2.95×10^{-8}

2.2. Simulation Setup

In this work, the color lattice Boltzmann model is used to simulate the two-phase flow during imbibition in porous media, which is efficiently implemented with the open-source LBPM software package (McClure et al., 2021). The color lattice Boltzmann model, with various advantages such as nonunitary viscosity ratio, adjustable interfacial tension, and narrower fluid interface, is commonly used to simulate multiphase flow in porous media to study the dynamics of the two-phase interface, fluid flow physics, and to calculate petrophysical properties such as capillary pressure and relative permeability (Huang et al., 2011; H. Liu et al., 2016). LBPM, equipped with various computational protocols and morphological and internal analysis tools, can easily mimic different flow processes at the pore scale and carry out in situ analysis of the flow processes in various aspects. It not only puts the color model from theory to practical application effectively but also provides a promising tool for the development of digital rock analysis experiments. The theoretical basis of the color lattice Boltzmann model and the implementation details of LBPM can be

Table 2
Flow Conditions

Case	lgCa	Q (mL/hr)		
		Bentheimer	Doddington	Ketton
1	−2.5	47.18	39.96	26.87
2	−3.0	14.92	12.63	8.50
3	−3.5	4.72	4.00	2.69
4	−4.0	1.49	1.26	0.85

found in the work of McClure et al. (2014). The ability of this numerical method in simulating corner flow and snap-off under the completely wetting condition ($\theta = 0°$) is validated in Supporting Information S1.

This work focuses on the displacement mechanism and in situ fluid distribution characteristics under the influence of pore structure and injection velocity. Therefore, the fluid properties and wetting conditions are kept consistent in all simulation cases. Among them, the viscosity of the invading fluid, that is, the wetting phase, is $\mu_w = 1.67\,\text{mPa}\cdot\text{s}$, which is 0.1 of that of the defending fluid. This viscosity ratio is a typically unfavorable condition. The densities of the two phases are the same, that is, $\rho = 1,000\,\text{kg/m}^3$, the interfacial tension is set to $\sigma = 42\,\text{mN/m}$. In the simulation, the wetting fluid is injected at a specific volume flow rate Q through the inlet buffer layer and displaces the nonwetting fluid that occupies the entire pore space at the initial state. Both fluids can discharge the computational domain through the outlet buffer layer until the saturation of the invading fluid no longer varies. In order to quantify the difference between flow conditions, the capillary number is introduced here. This dimensionless parameter quantifies the relative magnitude of the viscous and capillary forces in the system. Based on Darcy-scale volume-averaged and pore-scale flow rates, the following two forms of capillary number are commonly used:

$$\text{Ca}^* = \frac{\mu_i Q}{A\sigma} \tag{2}$$

$$\text{Ca} = \frac{\mu_i Q}{\phi A\sigma} \tag{3}$$

where A is the cross-sectional area of the computational domain along the flow direction and μ_i and σ are the viscosity of the invading fluid and interfacial tension, respectively. The two forms of capillary number originate from the difference in fluid flow space, the former based on the assumption that the medium is continuous and the latter considering that fluid flow occurs in the pore space. After the pioneering work of Lenormand et al. (1988), where a phase diagram was established using the former as a base variable, most subsequent work continued to follow this form of capillary number. Since the porosity of the three rock samples used in this work varied widely, Equation 3 was chosen to characterize the flow conditions in order to achieve the goal of examining corner flow under conditions where the average flow velocity within the pore space is the same for different samples. The imbibition process at different capillary numbers is easily achieved by controlling the injected volume flow rate. The logarithm of the capillary number in this work varies between −2.5 and −4.0. The flow rates set for different models in different cases are shown in Table 2. These flow conditions are also marked in the lg$M$ − lgCa* phase diagram, shown in Figure 2, to facilitate direct comparison with previous work.

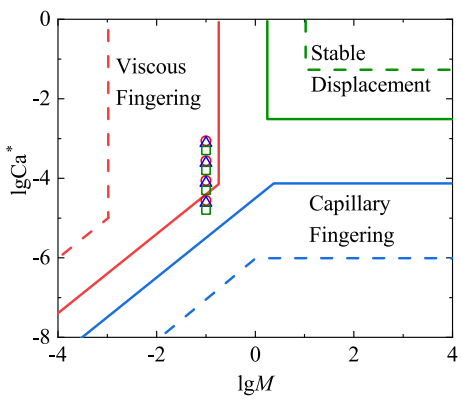

Figure 2. The different injection conditions in this work are indicated in the lg$M$-lgCa* phase diagram, where the hollow circles, triangles, and rectangles indicate the simulations of Bentheimer, Doddington, and Ketton, respectively. The regions corresponding to the different displacement patterns separated by dashed and solid lines were obtained by Lenormand et al. (1988) and C. Zhang et al. (2011), respectively.

3. Results and Discussion

3.1. Displacement Fronts Evolution

The morphological characteristics of the two-phase interface during imbibition are carefully examined from local to global based on visual observation of the phase field distribution. Taking the Ketton model as an example, Figure 3 shows the invading fluid distribution at equal time intervals (normalized by the time when the wetting fluid appears at the outlet at different flow rates). Since under the completely wetting condition, invading fluid flows preferentially along the solid surface at all Ca, as shown in the 2D slice in Figure 3. However, the local morphological characteristic shows some differences with Ca. At high Ca, the invading fluid completely fills the small pores, while in the large pores, it preferentially flows along a part of the solid surface, showing a certain film-like flow characteristic; at low Ca, the wetting fluid preferentially invades the corners and roughness of the pore space, forming

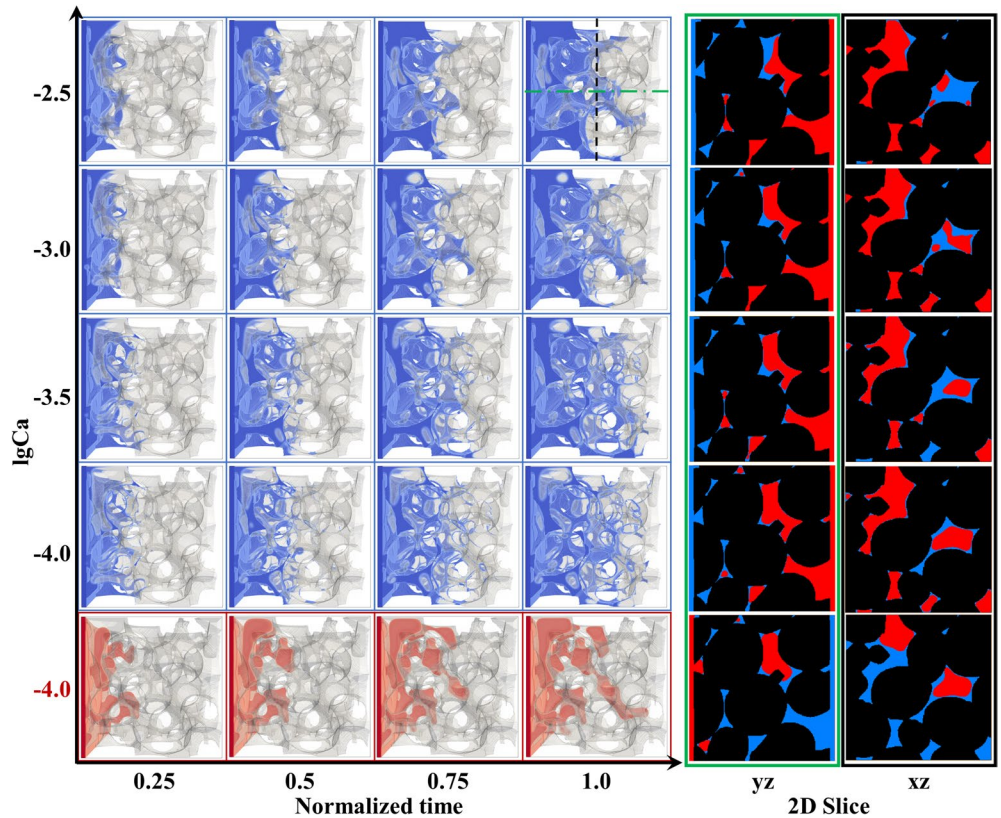

Figure 3. Evolution of displacement fronts within the Ketton model at different injection flow rates: the invading fluid distribution (blue boxes) at equal time intervals after normalizing the time with the breakthrough time, and 2D slices of the phase field distribution at breakthrough. The drainage simulation results (red boxes) for the same fluid properties at lgCa = −4.0 are additionally supplemented to demonstrate the morphological characteristics of the imbibition fronts, where blue and red indicate wetting and nonwetting fluids, respectively, and the extraction positions of yz and xz slices are shown as green and black dashed lines, respectively.

a corner flow-dominated flow characteristic. The overall morphological characteristic of the two-phase interface varies at different Ca. At high Ca, the invading fluid rapidly fills large pores, forming a preferential flow path, resulting in the displacement front exhibiting a viscous fingering morphological characteristic (invading fluid distribution at breakthrough); under low Ca, guided by the pore corner geometry, corner flow propagates along with all directions, and the displacement front, due to the hysteresis of the meniscus in the large pore (e.g., upper left corner of the model), have a rather rough morphology. This morphological characteristic contrasts with the displacement fronts (red boxes in Figure 3) during drainage under the same flow conditions and fluid properties. It is important to note that a small amount of corner flow still exists within some pores, even at relatively high Ca (lgCa = −3.0), due to the fully wetting and viscously unfavorable conditions and the complex pore structure. However, the corner flow under high Ca has a shorter length and a lower frequency of emergence, mainly distributed around the fingers with limited coverage. The length and frequency of the corner flow increase with decreasing Ca, which is consistent with the results observed in previous work (Dong & Chatzis, 2010).

The two-phase interface under the same flow conditions may exhibit different morphological characteristics due to the differences between the pore structures. Figure 4 shows the two-phase fluid distribution at breakthrough for the three models at different injection flow rates. At the highest Ca, the displacement front within all three porous media models exhibits a distinct viscous fingering morphology (black circle-marked area in Figure 4). However, the number of fingers varies between models, with the highest number in the Bentheimer model. As Ca decreases to lgCa = −3.0, the overall morphological characteristics of the displacement front for the three models begin to diverge. The fingers within the Doddington and Ketton models remain significant, while the fingers in the Bentheimer model, masked by its surrounding corner flow, can barely be observed directly. This difference is due to the Bentheimer model having a more curved pore-solid interface, which favors corner

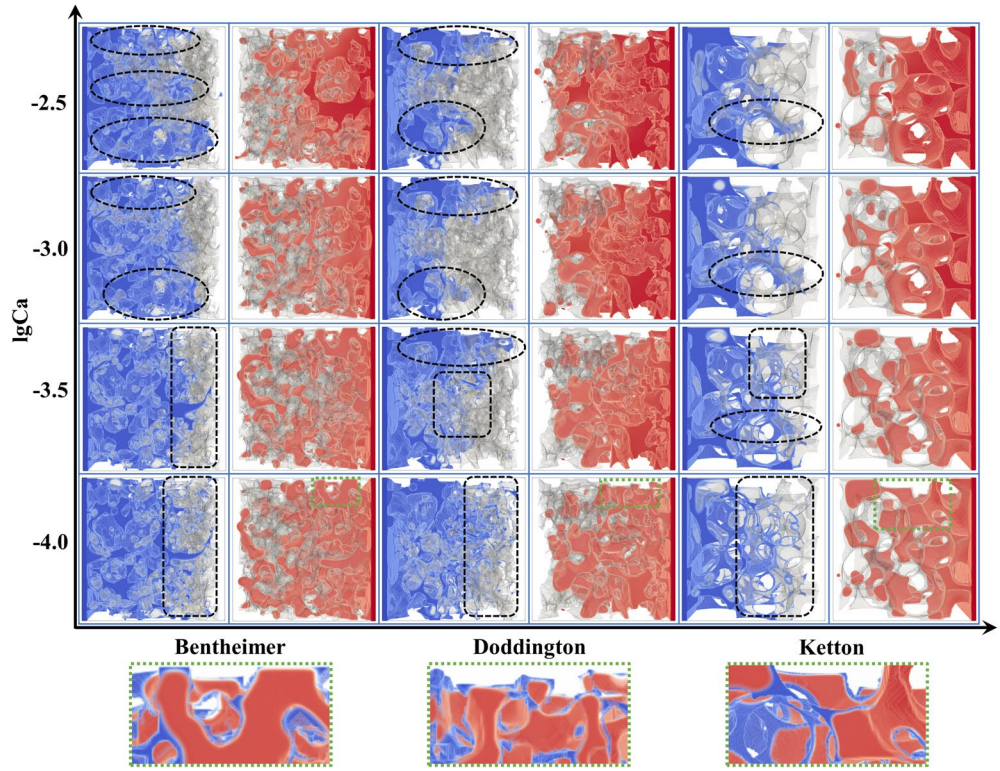

Figure 4. Two-phase fluid distribution at the breakthrough time for three models. Blue and red indicate wetting and nonwetting fluids, respectively, and gray indicates the pore-solid interface. The areas marked by the black circle and box roughly indicate the viscous fingering and corner flow areas, respectively. A zoomed-in view of the local area of the three samples at low Ca (green box marked area) is shown at the bottom to more visually demonstrate the corner flow characteristics.

flow. When further decreasing Ca to lgCa = −3.5, the difference in the morphology of the two-phase interface becomes more significant. Fingers remain evident in the Doddington model, weaken within the Ketton model, and disappear completely in the Bentheimer model. When decreasing Ca to the minimum value of this study, that is, lgCa = −4.0, the displacement front for all three models is dominated by corner flow (black box-marked area in Figure 4). Among them, the corner flow in the Ketton model is the most remarkable, where wetting fluid forms pendular rings at the grains' contact points and propagates within the pore space, eventually forming a chain of rings. This phenomenon has also been observed in microfluidic experiments (Scheel et al., 2008; Zhao et al., 2016).

3.2. Pore Filling Events

To further analyze the local dynamics of the two-phase interface, the pore-filling events during imbibition are separated into wetting and nonwetting fluid filling events. The former describes a pore space initially occupied by a nonwetting fluid and later filled by a wetting fluid, while the latter is the opposite (Ruecker et al., 2015). Based on the data containing phase-field distribution output at certain time intervals in the simulation, the pore-filling events of wetting and nonwetting fluids at different moments throughout the imbibition are extracted by comparing the changes of nonwetting fluid distribution in two consecutive data sets. Figure 5 shows the pore-filling event at a specific moment (expressed in the total injected fluid volume) in different simulations after injecting a wetting fluid of about 0.09 PV. It can be visually observed that the red marked area gradually decreases with decreasing Ca, indicating that the nonwetting fluid filling events are more at high Ca but less at low Ca. This is mainly due to the different pore-filling mechanisms. At high Ca, more discontinuous nonwetting fluids in the shape of droplets or clusters are mobilized due to the large viscous forces that can overcome Jamin's effect (Jamin, 1860), resulting in a large number of ganglion dynamics (marked by boxes). At low Ca, snap-off events (marked by triangles) are frequent, and nonwetting fluid filling events are mainly caused by the fluid

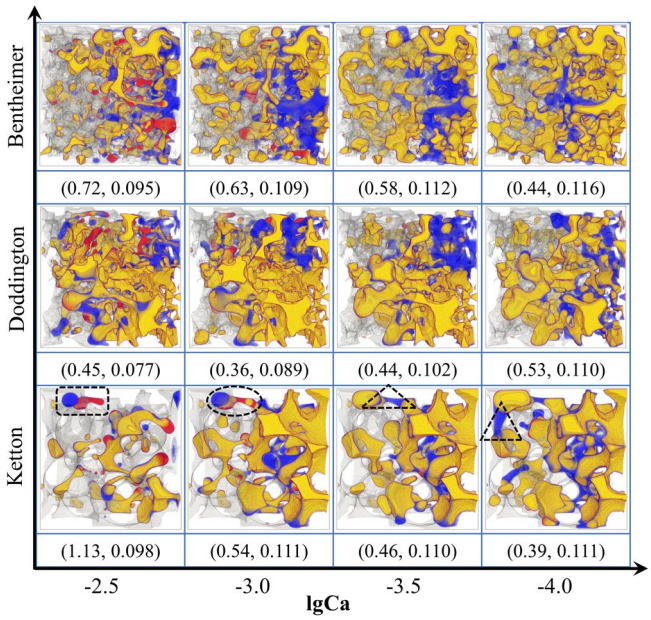

Figure 5. Pore filling events at a specific moment for different models: The two values in parentheses denote the total fluid volume injected at the current moment and the adjacent time interval, respectively, both scaled by the pore volume, that is, with a dimensionless unit of pore volume. Pore filling events are marked by different colors, where blue and red indicate wetting and nonwetting fluid filling events, respectively. In contrast, yellow indicates nonwetting fluids that have not changed in adjacent time intervals, and gray indicates pore-solid interfaces.

interfaces generated by the rapid contraction of the disconnected nonwetting phase. Eventually, this disconnected nonwetting phase is trapped in the center of the pore. The detailed dynamics of snap-off are described by Singh, Menke, et al. (2017). In contrast, the pore-filling mechanism at intermediate Ca seems to be a crossover between the first two scenarios. A continuous snap-off (marked by circles) can occur at a throat, accompanied by many moving droplets, but ultimately with little capillary trapping.

The nonwetting fluid filling events in imbibition are further quantified by calculating their volume ratio f_n relative to the injected fluid volume during adjacent time intervals, as shown in Figure 6. It can be seen that the f_n curves at different Ca show a trend of increasing and then decreasing with time, but their duration and occurrence both decrease with decreasing Ca. This is mainly due to the difference in the displacement pattern at different Ca, just like the analysis results in the previous section. In addition, the results in this section directly elucidate the reason for the high final recovery at high Ca, that is, the existence of a large number of nonwetting fluid filling events due to the ganglion dynamics dominating the flow at high Ca. Among these three models, the fluctuation in the f_n curve of the Ketton model is relatively higher due to its smaller pore volume and high clustering degree.

3.3. Microscopic Force Analysis

In order to investigate the dominant forces controlling imbibition under different flow rates, the pressure field distribution and the pressure difference ΔP between the inlet and outlet is recorded in detail. Figure 7 shows the pressure field normalized by the maximum and minimum pressure difference for different models at a specific moment before the breakthrough. Results show that the pressure field distribution characteristics are related to the position of the two-phase interface, and are significantly influenced by the injection flow rate. The pressure of both phases at different flow rates in the flow direction decreases gradually. At the two-phase interface, there is a significant pressure jump due to capillary pressure, that is, the pressure of the nonwetting fluid on one side of the interface is significantly higher than that of the wetting fluid on the other side. In addition, the pressure distributions on both sides of the interface are the lowest and highest pressure regions for the connected components of the wetting and nonwetting fluids, respectively. These results indicate that the imbibition process is influenced by both viscous and capillary forces over the range of injection flow rates imposed in this work. However, the relative magnitude of both forces controlling the flow varies with the injection rates. At high Ca, the overall distribution characteristics of the pressure field are less influenced by the interface position, and the minimum pressure is located at the outlet, indicating that the imbibition process under this condition is mainly dominated by viscous forces. The strength of capillary force controlling flow is progressively significant

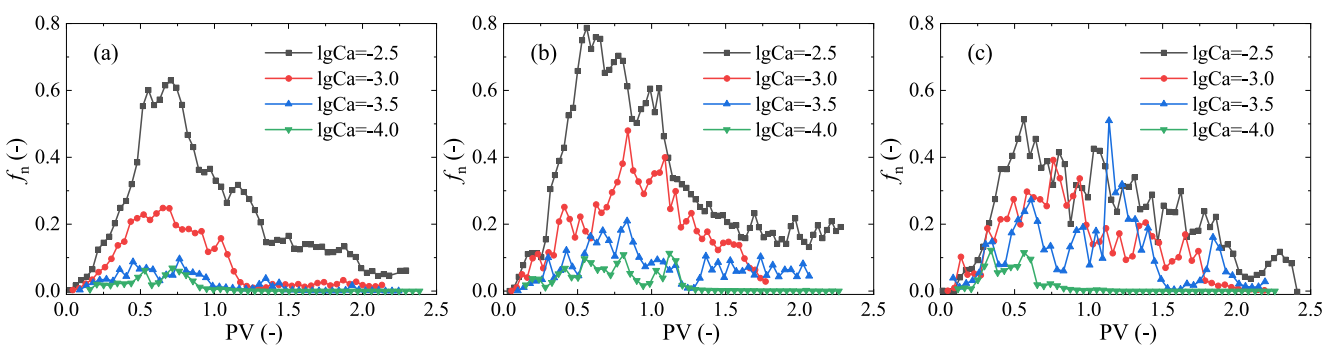

Figure 6. Quantification of nonwetting fluid filling events for the model of (a) Bentheimer, (b) Doddington, and (c) Ketton, where f_n is defined as the volume ratio of nonwetting fluid filling events in adjacent time intervals relative to the total injected fluid volume in that period.

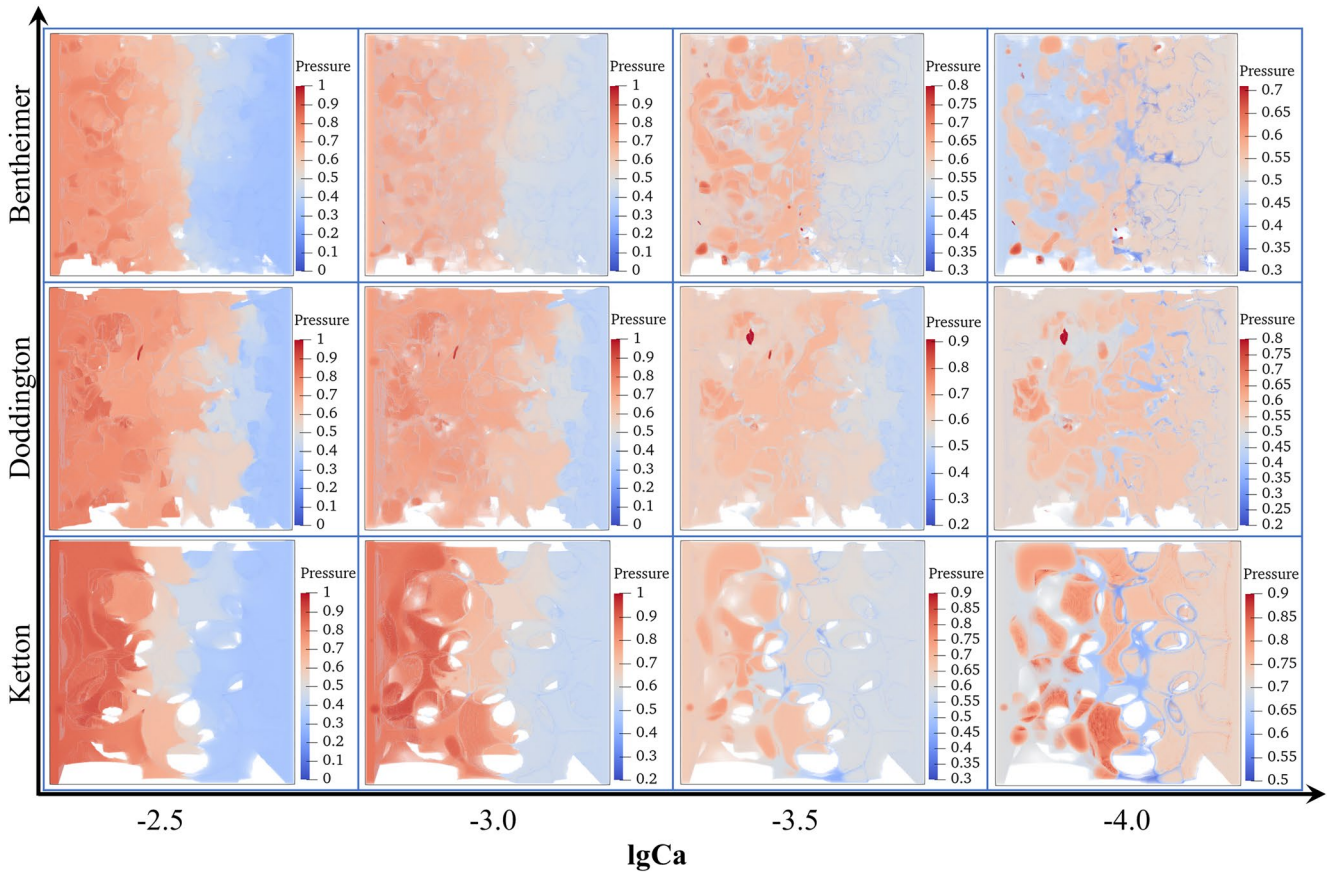

Figure 7. The normalized pressure field distribution at a specific moment before the breakthrough.

as Ca decreases. At low Ca, the overall distribution of the pressure field is obviously influenced by the interface position, the inlet pressure is significantly smaller than the outlet pressure, and the minimum value of the overall pressure field is located in the region occupied by the corner flow.

The variation of ΔP with injection volume (Figure 8) shows more visually the relative magnitude of capillary and viscous forces in the flow at different injection rates. For different models under the same Ca, the ΔP curves show an almost consistent trend, although there may be some differences in the displacement patterns. At the lowest Ca, ΔP is negative and remains almost constant before the displacement front disappears, indicating that the externally applied pressure acts as resistance during the displacement process. Thus, the capillary force is the dominant force controlling the flow under this displacement regime. The phenomenon has also been observed in

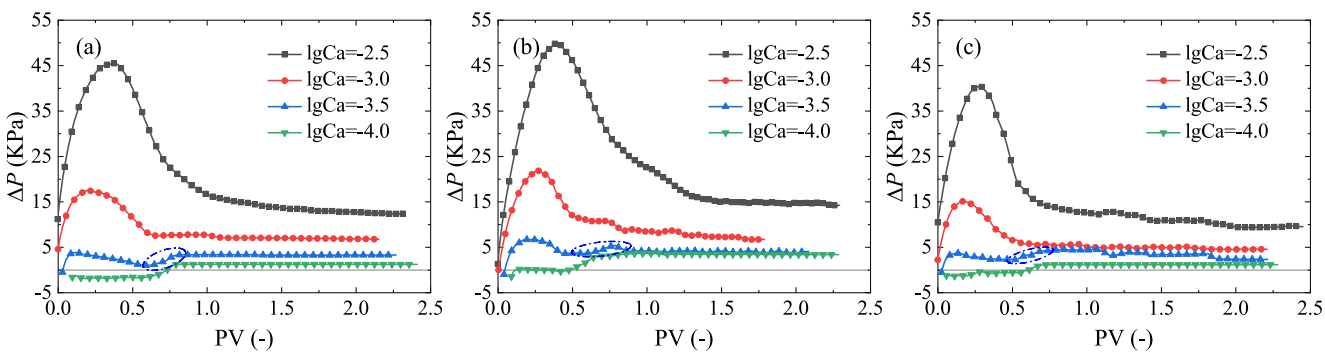

Figure 8. Variation of pressure difference ΔP with injected fluid volume pore volume for the model of (a) Bentheimer, (b) Doddington, and (c) Ketton. Where the blue circles indicate that the ΔP at that location shows an increasing trend.

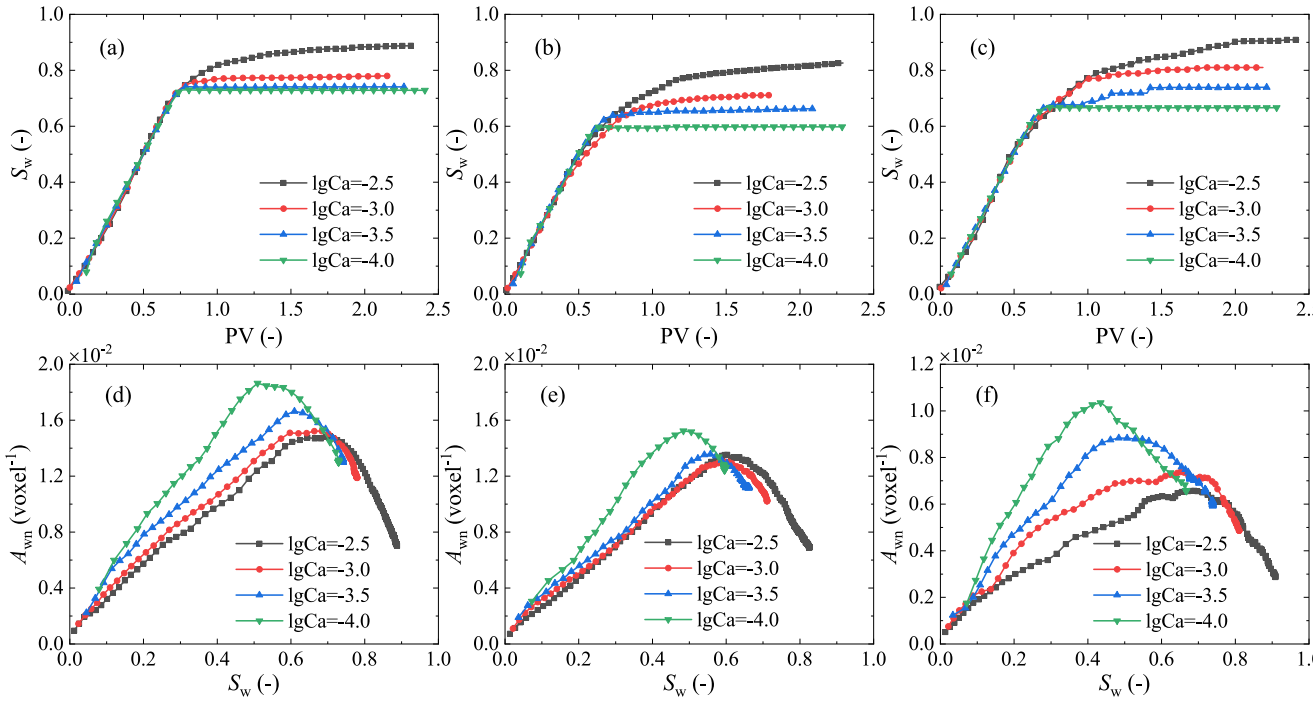

Figure 9. Two-phase fluid distribution characterization. (a–c) Variation of wetting fluid saturation S_w and (d–f) specific interface area A_{wn} during imbibition at different capillary numbers for the model of Bentheimer (left column), Doddington (middle column), and Ketton (right column).

previous work (Hu, Wu, et al., 2018). Note that the viscous force effect is still present under this condition, but its ability to control the flow is much weaker than the capillary force, as shown by the pressure field distribution under this condition in Figure 7. Under lgCa = −3.5, there is an increasing trend on the curve before ΔP reaches stability (marked by the blue circle in Figure 8). This is mainly related to the evolution of the imbibition front corresponding to this period. With the disappearance of the imbibition front, the capillary pressure on it, as a driving force, also disappears, thus requiring an additional energy input from external pressure. Since ΔP is always positive throughout the displacement at this Ca, viscous and capillary forces dominate the imbibition under this condition. At high Ca, ΔP gradually decreases with increasing injected volume of the low-viscosity fluid (scaled with pore volume, i.e., PV) and finally reaches a steady state, indicating that the viscous force is the dominant force in this displacement regime. In addition, before the breakthrough, a certain nonlinear relationship was found between ΔP and injection flux Q at the same saturation over the range of capillary numbers imposed in this work, shown in Figure S3 in Supporting Information S1. The nonlinear flow phenomenon observed in steady-state multiphase flow (Sinha & Hansen, 2012; Sinha et al., 2017; Tallakstad et al., 2009) also seems to appear during unsteady-state flow. Due to the limitation in the number of simulation cases and the range of capillary numbers, we will analyze the mechanism of this phenomenon during imbibition in future work.

3.4. Two-Phase Fluid Distribution

The two-phase fluid distribution in imbibition is quantitatively characterized from several aspects. First, the wetting fluid saturation S_w variation with PV is analyzed, as shown in Figures 9a–9c. Due to the imposed volumetric flow condition, the S_w curves at each Ca increase linearly by a certain degree and then diverge. S_w at low Ca rapidly reaches equilibrium, while S_w at high Ca increases slowly with fluid injection. Thus, the final saturation of the wetting fluid increases with increasing Ca. However, for Bentheimer, saturation curves at lgCa = −3.5 and −4.0 are almost identical due to the same imbibition regime for these two conditions. Previous work has also observed these trends in the saturation curves (McClure et al., 2021).

Then, the two-phase interface distribution characteristics are further analyzed, that is, the specific interface area A_{wn} at different S_w (Figures 9d–9f). The A_{wn} curves at each Ca shows a trend of increasing and then decreasing. This results from the combined effect of the occupancy degree and spatial distribution of the two-phase fluid.

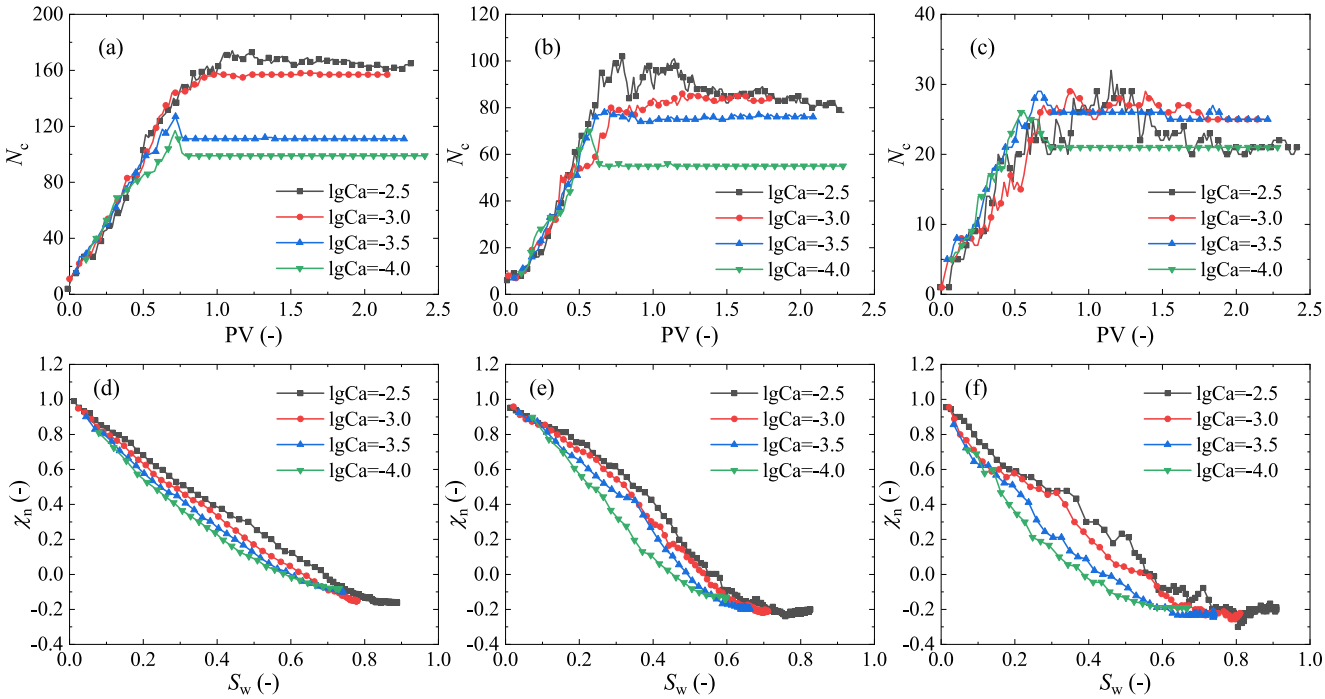

Figure 10. Fluid connectivity characterization. (a–c) Variation of cluster number N_c and (d–f) the pore space-normalized Euler characteristic χ_n of nonwetting fluid during imbibition at different capillary numbers for the model of Bentheimer (left column), Doddington (middle column), and Ketton (right column).

The maximum A_{wn} obtained at each Ca increases with decreasing Ca, and the saturation corresponding to the maximum A_{wn} increases with increasing Ca. The reason behind this phenomenon is due to the different displacement patterns under different Ca. In addition, the difference between pore structures can increase or decrease the difference of A_{wn} at different Ca at the same saturation.

3.5. Fluid Connectivity

The connectivity of the fluid within the pore space during imbibition, mainly through nonwetting fluid distribution due to its high clustering degree, is quantified from two perspectives. First, the changes in the cluster number of nonwetting fluid N_c during imbibition are monitored in detail (Figures 10a–10c). Before the terminal interface breakthrough, the N_c gradually increases with the injection of fluid. After the breakthrough, the N_c at low Ca remains constant and does not change anymore, while at high Ca, the N_c increases first due to the more significant viscous force that can overcome Jamin's effect, and then gradually decreases as the nonwetting phase is gradually discharged. At the same time, the N_c curves at high Ca show large fluctuations, indicating that the fluid flow under this condition is accompanied by a large amount of breakdown and coalesce of fragmented fluid clusters.

Next, the Euler characteristic of nonwetting fluid is measured and normalized by the Euler characteristic of pore space to evaluate the connectivity of the nonwetting phase in imbibition (Figures 10d–10f). At the initial state, the nonwetting fluid occupies the entire pore space. Thus, the best connectivity corresponds to that moment with a value of 1.0 for the pore space-normalized Euler characteristic χ_n (Herring et al., 2013, 2019). The connectivity of nonwetting fluid gradually decreases as the nonwetting fluid is discharged. All three models show such a trend at each Ca. Before the imbibition reaches the steady-state, the connectivity of the nonwetting fluid corresponding to the same S_w deteriorates sequentially with decreasing Ca. The phenomenon, of course, is related to the displacement pattern at different Ca. However, by observing the cluster number evolution (Figures 10a–10c) and combining it with the definition of the pore space-normalized Euler characteristic, it can be inferred that the more in-depth reason is that the redundant connections of the nonwetting fluid are broken to a different extent at different Ca. Specifically, as Ca decreases, the dominance of the corner flow during the flow increases, and more topological loops are disrupted due to snap-off. After imbibition reaches a steady-state, the connectivity of

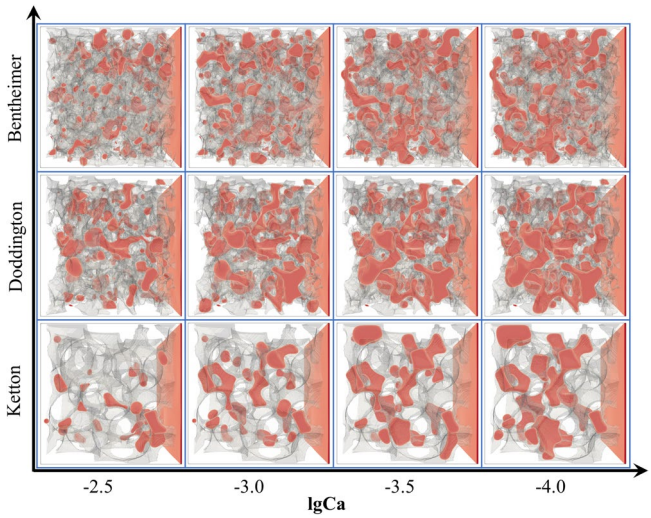

Figure 11. Nonwetting fluid clusters trapped in the pore space at the end of imbibition, where nonwetting fluid and pore-solid interface are shown in red and gray, respectively.

the nonwetting fluid at low Ca is better than that at high Ca due to the more significant number of large clusters at low Ca.

3.6. Nonwetting Fluid Residual Trapping

The distribution of the residual nonwetting fluid within the pore space after the end of imbibition is shown in Figure 11. The residual nonwetting fluid at high Ca is mainly located in the center of pore space as nearly spherical droplets, while at low Ca, it mainly occupies two or more adjacent pores in clusters. In addition, the size of isolated nonwetting fluid trapped at the exact location or in the same pore increases with decreasing Ca. This trend is more intuitively observed in the Ketton model.

To quantitatively evaluate the distribution characteristics of nonwetting fluids trapped in different types of porous media at different Ca, the cluster number $N(s)$ and cluster size s of the disconnected residual nonwetting fluids are counted, and the cumulative cluster-size distribution $S(s)$ is calculated according to the following relationship (Dias & Wilkinson, 1986):

$$S(s) = \sum_{s}^{\infty} \frac{sN(s)}{N_p} \tag{4}$$

where N_p denotes the number of voxels occupied by the pore space. Figure 12 represents $S(s)$ as a function of s in a log-log plot for the residual nonwetting fluid clusters in different models. Results indicate that cluster size under all Ca spans a wide range of nearly six orders of magnitude for all three models. In addition, $S(s)$ is almost constant for s less than a certain value (about 10^3 voxels and varies between model and Ca), while $S(s)$ decreases significantly for s greater than that value. This means that the number of large clusters is small, but their contribution to the overall saturation is significant, while the number of tiny droplets is large, but their contribution to the overall saturation is negligible. This is more consistent with the results observed in the micro-CT scanning experiment after imbibition (Iglauer et al., 2012).

4. Conclusions

In this work, forced imbibition in three natural rocks is simulated under the completely wetting and viscously unfavorable conditions based on the color lattice Boltzmann model. The two-phase interface and fluid structure during the whole displacement process are analyzed in detail and the following two conclusions are obtained:

1. Incomplete pore filling and nonwetting fluid ganglion are present at different injection flow rates, but the reasons behind them and their dynamics are different. This is mainly determined by the different flow characteristics of the invading fluid. At the high capillary number (lgCa = −2.5), ganglion dynamics dominate imbibition, due to the flow characteristic of the invading fluid flowing in leading films along a part of solid surface

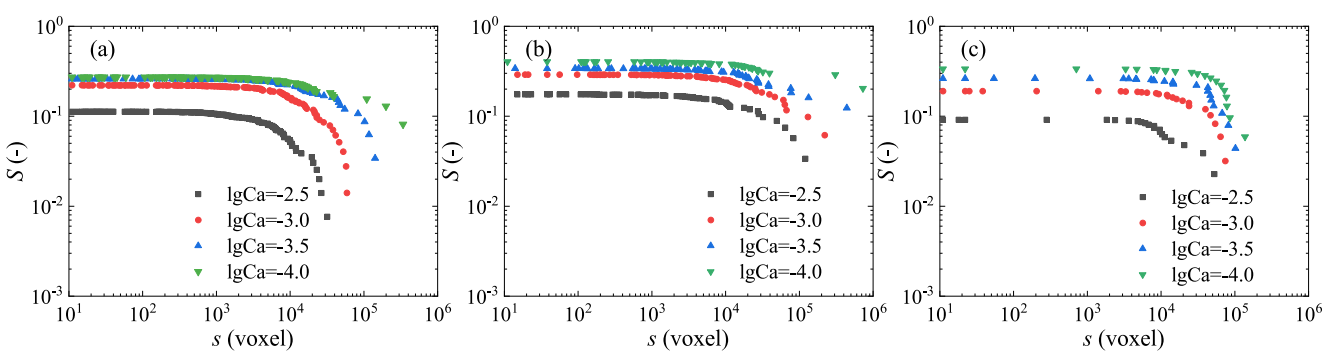

Figure 12. Nonwetting fluid residual cluster distributions as a function of cluster volume under different capillary numbers for the model of (a) Bentheimer, (b) Doddington, and (c) Ketton.

of large pores, as well as the effect of larger viscous forces. At the low capillary number (lgCa = −4.0), ganglion trapping dominates imbibition, due to corner flow and snap-off, and the effect of larger capillary forces.

2. The local filling dynamics and the overall morphology of the two-phase interface control the two-phase fluid distribution and fluid structure. As the capillary number, expressed in logarithms, varies from −2.5 to −4.0, the morphology of the displacement front changes from viscous fingering to a rough but uniform characteristic. Accordingly, before breakthrough, the two-phase interface increases, the connectivity becomes poor, the microscopic displacement efficiency decreases, and the final residual trapping increases. Pore structure only affects the magnitude of changes in these indicators, but not their trend over time.

The present work visualizes the rich flow physics and complex interfacial dynamics that occur in the pore space during imbibition as only a single factor changes, that is, the injection flow rate, and examines their effects on the overall structure and distribution of the fluids from multiple perspectives. These results help to deepen our understanding of the microscopic flow mechanisms behind the engineering applications such as oil resource exploitation and groundwater contamination remediation. It is also helpful to improve the research methods or theories related to multiphase flow in porous media, and may also help the upscaling studies under fully wetting conditions. For example, the effect of additional interfaces such as corner flow and film-like flow is included in the displacement rules in pore network modeling to more realistically reflect the actual flow process, and with the help of other methods, to more accurately predict the seepage characteristics at scales of engineering interest. Only a single and uniform wetting condition is considered in this work. However, the in situ wetting conditions in actual reservoirs are highly complex due to the spatial distribution of mineral composition, adsorption of polar substances in hydrocarbon, and the solid surface's roughness. Therefore, future work can focus on how wettability heterogeneity affects pore filling mechanisms and displacement patterns and can carry out a pore-by-pore analysis to better understand the microscopic flow mechanisms during immiscible displacement in porous media.

Data Availability Statement

Two-phase fluid distribution data for the Ketton model at different injection flow rates used in this study are deposited at https://doi.org/10.5281/zenodo.7081173. The open-source LBPM software package at https://github.com/OPM/LBPM is used in this study.

Acknowledgments
This work is supported by the National Natural Science Foundation of China (Grant No. 42172159) and the Fundamental Research Funds for the Central Universities (Grant Nos. 2462019YJRC011 and 2462021YXZZ005).

References

Abdallah, W., Buckley, J. S., Carnegie, A., Edwards, J., Herold, B., Fordham, E., et al. (2007). Fundamentals of wettability. *Schlumberger Oilfield Review*, *19*, 44–61.

Alhosani, A., Scanziani, A., Lin, Q., Foroughi, S., Alhammadi, A. M., Blunt, M. J., & Bijeljic, B. (2020). Dynamics of water injection in an oil-wet reservoir rock at subsurface conditions: Invasion patterns and pore-filling events. *Physical Review E*, *102*(2), 023110. https://doi.org/10.1103/physreve.102.023110

Armstrong, R. T., & Berg, S. (2013). Interfacial velocities and capillary pressure gradients during Haines jumps. *Physical Review E*, *88*(4), 043010. https://doi.org/10.1103/physreve.88.043010

Armstrong, R. T., Georgiadis, A., Ott, H., Klemin, D., & Berg, S. (2014). Critical capillary number: Desaturation studied with fast X-ray computed microtomography. *Geophysical Research Letters*, *41*(1), 55–60. https://doi.org/10.1002/2013gl058075

Armstrong, R. T., McClure, J. E., Berrill, M. A., Rücker, M., Schlüter, S., & Berg, S. (2016). Beyond Darcy's law: The role of phase topology and ganglion dynamics for two-fluid flow. *Physical Review E*, *94*(4), 043113. https://doi.org/10.1103/physreve.94.043113

Armstrong, R. T., McClure, J. E., Robins, V., Liu, Z., Arns, C. H., Schlueter, S., & Berg, S. (2019). Porous media characterization using Minkowski functionals: Theories, applications and future directions. *Transport in Porous Media*, *130*(1), 305–335. https://doi.org/10.1007/s11242-018-1201-4

Bakhshian, S., Rabbani, H. S., Hosseini, S. A., & Shokri, N. (2020). New insights into complex interactions between heterogeneity and wettability influencing two-phase flow in porous media. *Geophysical Research Letters*, *47*(14), e2020GL088187. https://doi.org/10.1029/2020gl088187

Berg, S., Ott, H., Klapp, S. A., Schwing, A., Neiteler, R., Brussee, N., et al. (2013). Real-time 3D imaging of Haines jumps in porous media flow. *Proceedings of the National Academy of Sciences of the United States of America*, *110*(10), 3755–3759. https://doi.org/10.1073/pnas.1221373110

Blunt, M. J. (2001). Flow in porous media—Pore-network models and multiphase flow. *Current Opinion in Colloid & Interface Science*, *6*(3), 197–207. https://doi.org/10.1016/s1359-0294(01)00084-x

Blunt, M. J. (2017). *Multiphase flow in permeable media: A pore-scale perspective*. Cambridge University Press.

Cai, J., Chen, Y., Liu, Y., Li, S., & Sun, C. (2022). Capillary imbibition and flow of wetting liquid in irregular capillaries: A 100-year review. *Advances in Colloid and Interface Science*, *304*, 102654. https://doi.org/10.1016/j.cis.2022.102654

Cai, J., Jin, T., Kou, J., Zou, S., Xiao, J., & Meng, Q. (2021). Lucas-Washburn equation-based modeling of capillary-driven flow in porous systems. *Langmuir*, *37*(5), 1623–1636. https://doi.org/10.1021/acs.langmuir.0c03134

Cai, J., Wood, D. A., Hajibeygi, H., & Iglauer, S. (2022). Multiscale and multiphysics influences on fluids in unconventional reservoirs: Modeling and simulation. *Advances in Geo-Energy Research*, *6*(2), 91–94. https://doi.org/10.46690/ager.2022.02.01

Chen, Y.-F., Wu, D.-S., Fang, S., & Hu, R. (2018). Experimental study on two-phase flow in rough fracture: Phase diagram and localized flow channel. *International Journal of Heat and Mass Transfer*, *122*, 1298–1307. https://doi.org/10.1016/j.ijheatmasstransfer.2018.02.031

Cieplak, M., & Robbins, M. O. (1988). Dynamical transition in quasistatic fluid invasion in porous media. *Physical Review Letters*, *60*(20), 2042–2045. https://doi.org/10.1103/physrevlett.60.2042

Cieplak, M., & Robbins, M. O. (1990). Influence of contact angle on quasistatic fluid invasion of porous media. *Physical Review B: Condensed Matter*, *41*(16), 11508–11521. https://doi.org/10.1103/physrevb.41.11508

Diao, Z., Li, S., Liu, W., Liu, H., & Xia, Q. (2021). Numerical study of the effect of tortuosity and mixed wettability on spontaneous imbibition in heterogeneous porous media. *Capillarity*, *4*(3), 50–62. https://doi.org/10.46690/capi.2021.03.02

Dias, M. M., & Wilkinson, D. (1986). Percolation with trapping. *Journal of Physics A: Mathematical and General*, *19*(15), 3131–3146. https://doi.org/10.1088/0305-4470/19/15/034

Dong, M., & Chatzis, I. (1995). The imbibition and flow of a wetting liquid along the corners of a square capillary tube. *Journal of Colloid and Interface Science*, *172*(2), 278–288. https://doi.org/10.1006/jcis.1995.1253

Dong, M., & Chatzis, I. (2010). Effect of capillary pressure on wetting film imbibition ahead of main liquid-gas displacement front in porous media. *Petroleum Science and Technology*, *28*(9), 955–968. https://doi.org/10.1080/10916460902937067

Gao, Y., Raeini, A. Q., Blunt, M. J., & Bijeljic, B. (2021). Dynamic fluid configurations in steady-state two-phase flow in Bentheimer sandstone. *Physical Review E*, *103*(1), 013110. https://doi.org/10.1103/physreve.103.013110

Geistlinger, H., & Zulfiqar, B. (2020). The impact of wettability and surface roughness on fluid displacement and capillary trapping in 2-D and 3-D porous media: 1. Wettability-controlled phase transition of trapping efficiency in glass beads packs. *Water Resources Research*, *56*(10), e2019WR026826. https://doi.org/10.1029/2019wr026826

Herring, A. L., Gilby, F., Li, Z., McClure, J., Turner, M., Veldkamp, J., et al. (2018). Observations of nonwetting phase snap-off during drainage. *Advances in Water Resources*, *121*, 32–43. https://doi.org/10.1016/j.advwatres.2018.07.016

Herring, A. L., Harper, E. J., Andersson, L., Sheppard, A., Bay, B. K., & Wildenschild, D. (2013). Effect of fluid topology on residual nonwetting phase trapping: Implications for geologic CO_2 sequestration. *Advances in Water Resources*, *62*, 47–58. https://doi.org/10.1016/j.advwatres.2013.09.015

Herring, A. L., Robins, V., & Sheppard, A. P. (2019). Topological persistence for relating microstructure and capillary fluid trapping in sandstones. *Water Resources Research*, *55*(1), 555–573. https://doi.org/10.1029/2018wr022780

Hu, R., Wan, J., Yang, Z., Chen, Y.-F., & Tokunaga, T. (2018). Wettability and flow rate impacts on immiscible displacement: A theoretical model. *Geophysical Research Letters*, *45*(7), 3077–3086. https://doi.org/10.1002/2017gl076600

Hu, R., Wu, D.-S., Yang, Z., & Chen, Y.-F. (2018). Energy conversion reveals regime transition of imbibition in a rough fracture. *Geophysical Research Letters*, *45*(17), 8993–9002. https://doi.org/10.1029/2018gl079302

Huang, H., Wang, L., & Lu, X.-Y. (2011). Evaluation of three lattice Boltzmann models for multiphase flows in porous media. *Computers & Mathematics with Applications*, *61*(12), 3606–3617. https://doi.org/10.1016/j.camwa.2010.06.034

Iglauer, S., Ferno, M. A., Shearing, P., & Blunt, M. J. (2012). Comparison of residual oil cluster size distribution, morphology and saturation in oil-wet and water-wet sandstone. *Journal of Colloid and Interface Science*, *375*(1), 187–192. https://doi.org/10.1016/j.jcis.2012.02.025

Jamin, J. (1860). Memoire sur l'equilibre et le mouvement des liquides dans les corps poreux. *Comptes Rendus Academie de Sciences de France*, *50*, 172–176.

Jung, M., Brinkmann, M., Seemann, R., Hiller, T., de la Lama, M. S., & Herminghaus, S. (2016). Wettability controls slow immiscible displacement through local interfacial instabilities. *Physical Review Fluids*, *1*(7), 074202. https://doi.org/10.1103/physrevfluids.1.074202

Khanamiri, H. H., & Torsæter, O. (2018). Fluid topology in pore scale two-phase flow imaged by synchrotron X-ray microtomography. *Water Resources Research*, *54*(3), 1905–1917. https://doi.org/10.1002/2017wr021302

Kubochkin, N., & Gambaryan-Roisman, T. (2022). Capillary-driven flow in corner geometries. *Current Opinion in Colloid & Interface Science*, *59*, 101575. https://doi.org/10.1016/j.cocis.2022.101575

Legland, D., Kieu, K., & Devaux, M. F. (2007). Computation of Minkowski measures on 2D and 3D binary images. *Acta Stereologica*, *26*(2), 83–92. https://doi.org/10.5566/ias.v26.p83-92

Lenormand, R. (1990). Liquids in porous-media. *Journal of Physics: Condensed Matter*, *2*(S), SA79–SA88. https://doi.org/10.1088/0953-8984/2/s/008

Lenormand, R., Touboul, E., & Zarcone, C. (1988). Numerical models and experiments on immiscible displacements in porous media. *Journal of Fluid Mechanics*, *189*, 165–187. https://doi.org/10.1017/s0022112088000953

Liu, H., Kang, Q., Leonardi, C. R., Schmieschek, S., Narvaez, A., Jones, B. D., et al. (2016). Multiphase lattice Boltzmann simulations for porous media applications. *Computational Geosciences*, *20*(4), 777–805. https://doi.org/10.1007/s10596-015-9542-3

Liu, H., Zhu, Z., Patrick, W., Liu, J., Lei, H., & Zhang, L. (2020). Pore-scale numerical simulation of supercritical CO_2 migration in porous and fractured media saturated with water. *Advances in Geo-Energy Research*, *4*(4), 419–434. https://doi.org/10.46690/ager.2020.04.07

Liu, Y., Iglauer, S., Cai, J., Amooie, M. A., & Qin, C. (2019). Local instabilities during capillary-dominated immiscible displacement in porous media. *Capillarity*, *2*(1), 1–7. https://doi.org/10.26804/capi.2019.01.01

McClure, J. E., Li, Z., Berrill, M., & Ramstad, T. (2021). The LBPM software package for simulating multiphase flow on digital images of porous rocks. *Computational Geosciences*, *25*(3), 871–895. https://doi.org/10.1007/s10596-020-10028-9

McClure, J. E., Prins, J. F., & Miller, C. T. (2014). A novel heterogeneous algorithm to simulate multiphase flow in porous media on multicore CPU-GPU systems. *Computer Physics Communications*, *185*(7), 1865–1874. https://doi.org/10.1016/j.cpc.2014.03.012

Meisenheimer, D. E., McClure, J. E., Rivers, M. L., & Wildenschild, D. (2020). Exploring the effect of flow condition on the constitutive relationships for two-phase flow. *Advances in Water Resources*, *137*, 103506. https://doi.org/10.1016/j.advwatres.2020.103506

Michels, R., Siebert, D. N., & Emerich dos Santos, L. O. (2021). Investigation on the influence of capillary number on drainage in porous media using a lattice Boltzmann method. *Journal of Petroleum Science & Engineering*, *205*, 108918. https://doi.org/10.1016/j.petrol.2021.108918

Mohanty, K. K., Davis, H. T., & Scriven, L. (1987). Physics of oil entrapment in water-wet rock. *SPE Reservoir Engineering*, *2*(01), 113–128. https://doi.org/10.2118/9406-pa

Morrow, N. R. (1970). Physics and thermodynamics of capillary action in porous media. *Industrial & Engineering Chemistry*, *62*(6), 32–56. https://doi.org/10.1021/ie50726a006

Pak, T., Butler, I. B., Geiger, S., Van Dijke, M. I., & Sorbie, K. S. (2015). Droplet fragmentation: 3D imaging of a previously unidentified pore-scale process during multiphase flow in porous media. *Proceedings of the National Academy of Sciences of the United States of America*, *112*(7), 1947–1952. https://doi.org/10.1073/pnas.1420202112

Porter, M. L., Schaap, M. G., & Wildenschild, D. (2009). Lattice-Boltzmann simulations of the capillary pressure–saturation–interfacial area relationship for porous media. *Advances in Water Resources*, *32*(11), 1632–1640. https://doi.org/10.1016/j.advwatres.2009.08.009

Raeini, A. Q., Bijeljic, B., & Blunt, M. J. (2017). Generalized network modeling: Network extraction as a coarse-scale discretization of the void space of porous media. *Physical Review E*, *96*(1), 013312. https://doi.org/10.1103/physreve.96.013312

Reynolds, C. A., Menke, H., Andrew, M., Blunt, M. J., & Krevor, S. (2017). Dynamic fluid connectivity during steady-state multiphase flow in a sandstone. *Proceedings of the National Academy of Sciences of the United States of America*, *114*(31), 8187–8192. https://doi.org/10.1073/pnas.1702834114

Roof, J. (1970). Snap-off of oil droplets in water-wet pores. *Society of Petroleum Engineers Journal*, *10*(1), 85–90. https://doi.org/10.2118/2504-pa

Ruecker, M., Berg, S., Armstrong, R. T., Georgiadis, A., Ott, H., Schwing, A., et al. (2015). From connected pathway flow to ganglion dynamics. *Geophysical Research Letters*, *42*(10), 3888–3894. https://doi.org/10.1002/2015gl064007

Scheel, M., Seemann, R., Brinkmann, M., Di Michiel, M., Sheppard, A., Breidenbach, B., & Herminghaus, S. (2008). Morphological clues to wet granular pile stability. *Nature Materials*, *7*(3), 189–193. https://doi.org/10.1038/nmat2117

Schlüter, S., Berg, S., Rücker, M., Armstrong, R., Vogel, H. J., Hilfer, R., & Wildenschild, D. (2016). Pore-scale displacement mechanisms as a source of hysteresis for two-phase flow in porous media. *Water Resources Research*, *52*(3), 2194–2205. https://doi.org/10.1002/2015wr018254

Sergi, D., Grossi, L., Leidi, T., & Ortona, A. (2016). Simulation of capillary infiltration into packing structures for the optimization of ceramic materials using the lattice Boltzmann method. *Engineering Applications of Computational Fluid Mechanics*, *10*(1), 485–499. https://doi.org/10.1080/19942060.2016.1189361

Singh, K., Jung, M., Brinkmann, M., & Seemann, R. (2019). Capillary-dominated fluid displacement in porous media. *Annual Review of Fluid Mechanics*, *51*(1), 429–449. https://doi.org/10.1146/annurev-fluid-010518-040342

Singh, K., Menke, H., Andrew, M., Lin, Q., Rau, C., Blunt, M. J., & Bijeljic, B. (2017). Dynamics of snap-off and pore-filling events during two-phase fluid flow in permeable media. *Scientific Reports*, *7*(1), 5192. https://doi.org/10.1038/s41598-017-05204-4

Singh, K., & Niven, R. K. (2013). Non-aqueous phase liquid spills in freezing and thawing soils: Critical analysis of pore-scale processes. *Critical Reviews in Environmental Science and Technology*, *43*(6), 551–597. https://doi.org/10.1080/10643389.2011.604264

Singh, K., Scholl, H., Brinkmann, M., Di Michiel, M., Scheel, M., Herminghaus, S., & Seemann, R. (2017). The role of local instabilities in fluid invasion into permeable media. *Scientific Reports*, *7*(1), 444. https://doi.org/10.1038/s41598-017-00191-y

Sinha, S., Bender, A. T., Danczyk, M., Keepseagle, K., Prather, C. A., Bray, J. M., et al. (2017). Effective rheology of two-phase flow in three-dimensional porous media: Experiment and simulation. *Transport in Porous Media*, *119*(1), 77–94. https://doi.org/10.1007/s11242-017-0874-4

Sinha, S., & Hansen, A. (2012). Effective rheology of immiscible two-phase flow in porous media. *Europhysics Letters*, *99*(4), 44004. https://doi.org/10.1209/0295-5075/99/44004

Spurin, C., Bultreys, T., Rücker, M., Garfi, G., Schlepütz, C. M., Novak, V., et al. (2021). The development of intermittent multiphase fluid flow pathways through a porous rock. *Advances in Water Resources*, *150*, 103868. https://doi.org/10.1016/j.advwatres.2021.103868

Sun, Z. (2018). *Capillary phenomena in porous media: Pore and grain scale studies*. Georgia Institute of Technology.

Tallakstad, K. T., Knudsen, H. A., Ramstad, T., Løvoll, G., Måløy, K. J., Toussaint, R., & Flekkøy, E. G. (2009). Steady-state two-phase flow in porous media: Statistics and transport properties. *Physical Review Letters*, *102*(7), 074502. https://doi.org/10.1103/physrevlett.102.074502

Tsuji, T., Jiang, F., & Christensen, K. T. (2016). Characterization of immiscible fluid displacement processes with various capillary numbers and viscosity ratios in 3D natural sandstone. *Advances in Water Resources*, *95*, 3–15. https://doi.org/10.1016/j.advwatres.2016.03.005

Wiklund, H. S., & Uesaka, T. (2013). Microfluidics of imbibition in random porous media. *Physical Review E*, *87*(2), 023006. https://doi.org/10.1103/physreve.87.023006

Wilkinson, D., & Willemsen, J. F. (1983). Invasion percolation: A new form of percolation theory. *Journal of Physics A: Mathematical and General*, *16*(14), 3365–3376. https://doi.org/10.1088/0305-4470/16/14/028

Wu, R., Kharaghani, A., & Tsotsas, E. (2016). Two-phase flow with capillary valve effect in porous media. *Chemical Engineering Science*, *139*, 241–248. https://doi.org/10.1016/j.ces.2015.09.028

Xu, Z., Liu, H., & Valocchi, A. J. (2017). Lattice Boltzmann simulation of immiscible two-phase flow with capillary valve effect in porous media. *Water Resources Research*, *53*(5), 3770–3790. https://doi.org/10.1002/2017wr020373

Zacharoudiou, I., Boek, E. S., & Crawshaw, J. (2018). The impact of drainage displacement patterns and Haines jumps on CO_2 storage efficiency. *Scientific Reports*, *8*(1), 1. https://doi.org/10.1038/s41598-018-33502-y

Zhang, C., Oostrom, M., Wietsma, T. W., Grate, J. W., & Warner, M. G. (2011). Influence of viscous and capillary forces on immiscible fluid displacement: Pore-scale experimental study in a water-wet micromodel demonstrating viscous and capillary fingering. *Energy & Fuels*, *25*(8), 3493–3505. https://doi.org/10.1021/ef101732k

Zhang, Y., Bijeljic, B., Gao, Y., Lin, Q., & Blunt, M. J. (2021). Quantification of nonlinear multiphase flow in porous media. *Geophysical Research Letters*, *48*(5), e2020GL090477. https://doi.org/10.1029/2020gl090477

Zhao, B., MacMinn, C. W., & Juanes, R. (2016). Wettability control on multiphase flow in patterned microfluidics. *Proceedings of the National Academy of Sciences of the United States of America*, *113*(37), 10251–10256. https://doi.org/10.1073/pnas.1603387113